



**HAL**  
open science

## Phase transformation of the Ti-5553 titanium alloy subjected to rapid heating

Nicolas Chanfreau, Dominique Poquillon, Andreas Stark, Emad Maawad,  
Charles Mareau, Moukrane Dehmas

► **To cite this version:**

Nicolas Chanfreau, Dominique Poquillon, Andreas Stark, Emad Maawad, Charles Mareau, et al..  
Phase transformation of the Ti-5553 titanium alloy subjected to rapid heating. *Journal of Materials  
Science*, 2022, *Metals & corrosion*, 57 (9), pp.5620-5633. 10.1007/s10853-022-06959-6 . hal-03881454

**HAL Id: hal-03881454**

**<https://hal.science/hal-03881454>**

Submitted on 1 Dec 2022


**HAL** is a multi-disciplinary open access archive for the deposit and dissemination of scientific research documents, whether they are published or not. The documents may come from teaching and research institutions in France or abroad, or from public or private research centers.

L'archive ouverte pluridisciplinaire **HAL**, est destinée au dépôt et à la diffusion de documents scientifiques de niveau recherche, publiés ou non, émanant des établissements d'enseignement et de recherche français ou étrangers, des laboratoires publics ou privés.



Distributed under a Creative Commons Attribution 4.0 International License

# Phase transformation of the Ti-5553 titanium alloy subjected to rapid heating

Nicolas Chanfreau<sup>1,\*</sup> , Dominique Poquillon<sup>1</sup>, Andreas Stark<sup>2</sup>, Emad Maawad<sup>2</sup>, Charles Mareau<sup>3</sup>, and Moukrane Dehmas<sup>1</sup>

<sup>1</sup>CIRIMAT, CNRS, Université de Toulouse, INP- ENSIACET 4 allée Emile Monso, BP44362, 31030 Toulouse Cedex 4, France

<sup>2</sup>Institute of Materials Physics, Helmholtz-Zentrum Geesthacht, Max Plank Strasse 1, 21502 Geesthacht, Germany

<sup>3</sup>Laboratoire Angevin de Mécanique, Procédés et innovAtion, 2 Boulevard du Ronceray, Angers, France

---

## ABSTRACT

The  $\alpha \rightarrow \beta$  phase transformation upon heating in the Ti-5553 alloy with lamellar-nodular bimodal microstructure was tracked in situ with high energy X-ray diffraction. Rapid heating at 10, 50 and 100 °C s<sup>-1</sup> from room temperature to 1050 °C was tested. Phase transformation on heating was studied by a combined analysis of the microstructural features that provides estimates of mass fractions, mean lattice parameters and full width at half maximum for the two phases. In comparison with equilibrium conditions, the experimental mass fractions reveal a shift of the transformation domain toward high temperatures when the heating rate increases. Also, the dissolution of the  $\alpha$  phase is largely impacted by its morphology, the transformation being faster for  $\alpha$  lamellae. The combined analysis of mean lattice parameters and full width at half maximum suggests that the  $\alpha \rightarrow \beta$  phase transformation on heating is diffusion controlled. The  $\beta$  phase therefore inherits the solute content of the adjacent parent  $\alpha$  phase, leading to chemical heterogeneities in the  $\beta$  phase regardless of the heating rate.

---

## Introduction

Titanium alloys are widely used for the development of new aircrafts due to their high strength, low density, damage tolerance and corrosion resistance [1]. The microstructure of titanium alloys is known to have a significant impact on their mechanical properties [2, 3]. Some fabrication processes used for

titanium alloys, including induction heating [4], rapid heat treatments [5], welding [6, 7] and machining [8, 9], involve high heating rates. It is therefore important to understand the impact of the heating rate on the microstructure and the resulting mechanical properties of titanium alloys. The influence of the heating rate on phase transformation kinetics in  $\alpha + \beta$  titanium alloys has been studied by different authors [10–13]. Specifically, the dissolution

Address correspondence to E-mail: nicolas.chanfreau@toulouse-inp.fr

<https://doi.org/10.1007/s10853-022-06959-6>

kinetics of the  $\alpha$  phase in the Ti-6Al-4V alloy has been shown to be rapid [14], and Idhil Ismail et al. have shown that the  $\alpha$  phase dissolution can take place up to  $200\text{ }^{\circ}\text{C s}^{-1}$  [15]. In the case of  $\beta$ -metastable alloys, most of the literature focuses on the precipitation sequence [16–22] of the  $\alpha$  phase and the partitioning of solute elements during aging [23, 24]. The work of Callegari et al. [25] addresses the  $\alpha \rightarrow \beta$  transformation upon heating up to the  $\beta$  temperature domain. However, they have focused on the transformation sequence below  $500\text{ }^{\circ}\text{C}$  with low to intermediate heating rates ( $< 100\text{ }^{\circ}\text{C min}^{-1}$ ). Gridnev et al. [26] have studied the impact of the heating rate on the  $\beta$  transus temperature on various titanium alloys with either a fully lamellar or a fully nodular microstructure. This consideration prompted the present study, which focuses on the impact of the heating rate on the  $\alpha \rightarrow \beta$  phase transformation kinetics in the Ti-5553 titanium alloy with a bimodal microstructure. This alloy is commonly used for structural parts and landing gear in aerospace applications. For this purpose, in situ High Energy X-Ray Diffraction (HE-XRD) is used to evaluate the mass fractions, mean lattice parameters and full width at half maximum of the different phases as a function of temperature for heating rates ranging between  $10$  and  $100\text{ }^{\circ}\text{C s}^{-1}$ . From this experimental data, the role of solute elements diffusion on the  $\alpha \rightarrow \beta$  phase transformation upon heating is discussed.

## Material and methods

### Material and metallographic observations

The Ti-5553  $\beta$ -metastable alloy used in the present study has been supplied by Titanium Metals Corporation (TIMET Savoie). The measured chemical composition in mass% is 5.6Al, 5.2 V, 4.8Mo, 3.0Cr, 0.15O and balance Ti. According to metallographic observations, the  $\beta$  transus temperature ( $T_{\beta}$ ) was determined to be  $861\text{ }^{\circ}\text{C}$ .

The as-received microstructure has been observed without prior etching by scanning electron microscopy (SEM) a LEO435VP SEM in backscattered electron mode (BSE). The microstructural features have then been determined by image analysis using the ImageJ program [27] from 25 BSE-SEM images.

### In situ high energy X-ray diffraction

Phase transformations throughout rapid heating were tracked in situ with HE-XRD. The experiments have been carried out at the P07 beamline (operated by the Helmholtz-Zentrum Geesthacht) of the PETRA III facility [28, 29]. During the different experiments, cylindrical specimens (with a length of 10 mm and a diameter of 6 mm) have been heated under secondary vacuum in a DIL805A/D dilatometer (TA Instruments) equipped with an induction coil. The specimen temperature has been controlled with a calibrated S-type thermocouple spot-welded to the external surface. A similar heat treatment, which consists of heating with a constant rate ( $10\text{ }^{\circ}\text{C s}^{-1}$ ,  $50\text{ }^{\circ}\text{C s}^{-1}$  or  $100\text{ }^{\circ}\text{C s}^{-1}$ ) from room temperature to about  $1050\text{ }^{\circ}\text{C}$ , has been used for each specimen.

To gain insight into the microstructural transformations during heating, specimens have been illuminated by a monochromatic X-ray beam of 100 keV (wavelength of 0.01239 nm) with a cross section of  $1 \times 1\text{ mm}^2$  during heating. Because of the large penetration depth, the Debye–Scherrer rings have been collected in transmission mode on a 2D PerkinElmer XRD1621 detector with a resolution of 2048 by 2048 pixels and  $200\text{ }\mu\text{m}$  pixel size. The detector has been placed 1517 mm away from the sample. The resulting scattering angle  $2\theta$  is comprised between  $0^{\circ}$  and  $10.9^{\circ}$ . Raw 2D images of Debye–Scherrer rings have then been circularly integrated using the Fit2D program, after calibration with a  $\text{LaB}_6$  sample, to obtain intensity versus  $2\theta$  diffraction patterns. All diffraction patterns have been fitted with Pseudo-Voigt function, with the Rietveld method [30, 31] using the batch processing features of the WinPLOTR (FullProf suite) program [32]. The Rwp% [31] value for all fitted diffractogram was below 10%. As an example, the experimental and calculated diffraction patterns for the as-received state are compared in Fig. 1. All diffraction data are plotted against the norm of the scattering vector  $|G| = 4\pi \cdot \sin(\theta)/\lambda$ .

Following the Rietveld refinement, the mass fractions and mean lattice parameters for both  $\alpha$  and  $\beta$  phases, as well as full width at half maximum (FWHM) of  $\{10\bar{1}0\}_{\alpha}$ ,  $\{200\}_{\beta}$  peaks have been extracted. The FWHM for both peaks has been calculated with the simplified Caglioti's formula ( $\text{FWHM} = \sqrt{U^2 \tan^2(\theta) + V \tan(\theta) + W}$ ) [30, 33], with  $U$ ,  $V$  and  $W$  the fitted parameters by the Rietveld

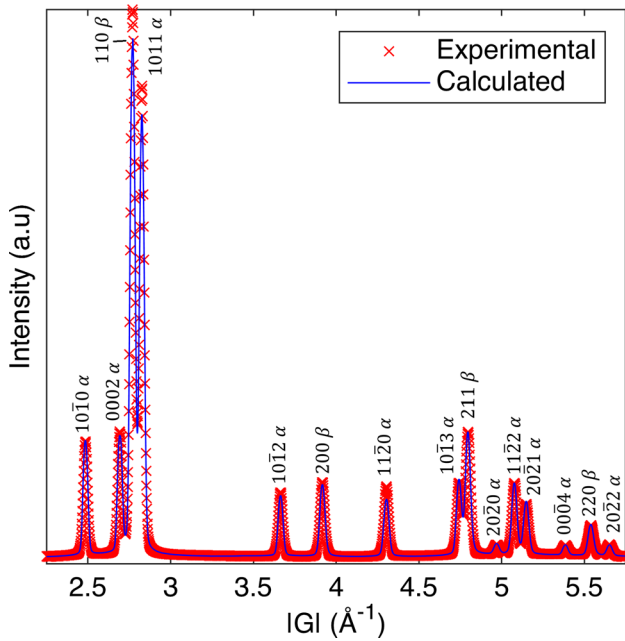


**Figure 1** Calculated via Rietveld refinement and experimental XRD patterns obtained at initial state. Only the fitted peaks are shown.

method. These peaks have been chosen for their well-defined shapes as well as the fact that they do not overlap with any other peak. Furthermore, the absence of  $hkl$ -dependence of peaks widths [34] has been verified by checking that the simplified Caglioti's formula predicted well the FWHM of all peaks. For the calculation of the mass fractions, the chemical composition of the phases at thermodynamic equilibrium at 600 °C for both phases was considered using ThermoCalc<sup>®</sup> software [35] and the Saunders database [36].

The acquisition frequency of the images has been fixed to 10 Hz, which corresponds to one recording every 10 °C in the case of the fastest heating rate (100 °C s<sup>-1</sup>).

## Results

### Initial microstructure

Figure 2 shows the typical microstructure of the as-received alloy. As a result of the processing conditions, the microstructure mainly consists of nodular  $\alpha$  phase (a) and fine  $\alpha$ -phase lamellae (b) embedded in the  $\beta$  matrix. The presence of a continuous layer of  $\alpha$  phase along the subgrain boundaries (c) should also

be noted. Lastly, a Precipitate Free Zone (PFZ) with an average thickness of 400 nm surrounding the  $\alpha$  nodular morphology was observed. The presence of a PFZ is explained by the local enrichment of the  $\beta$  phase in  $\beta$ -stabilizer elements during the growth of  $\alpha$  nodular phase. From a quantitative point of view, the  $\alpha$  nodules have an average equivalent diameter of 3.5  $\mu$ m. The length of the fine  $\alpha$  lamellae does not exceed 700 nm and their thickness is at most a few tens of nanometer. The thickness of the continuous layer of  $\alpha$  phase is about 0.4  $\mu$ m. Finally, an image analysis algorithm has been used to determine the mass fraction of the  $\alpha$  nodules. The algorithm allows removing the fine  $\alpha$  precipitates by opening. An opening example is shown in Fig. 3. According to image analysis, the mass fraction of nodular  $\alpha$  phase is 21%.

The total mass fraction of  $\alpha$  phase at room temperature has been determined by Rietveld refinement from synchrotron data. According to the Rietveld refinement, the total fraction of  $\alpha$  phase is about 56% for the samples heated at 50 and 100 °C s<sup>-1</sup> and 58% for the sample heated at 10 °C s<sup>-1</sup>. Though, the samples have been taken from the same billet area, slight differences regarding phase fractions are observed. The mass fraction of lamellar and grain boundaries  $\alpha$  precipitates (b and c type in Fig. 2) have been estimated by subtracting the nodular  $\alpha$  fraction determined by image analysis from the total mass fraction of  $\alpha$  phase. The resulting mass fraction of lamellar and grain boundaries  $\alpha$  precipitates is about 35% (37% for the sample heated at 10 °C s<sup>-1</sup>).

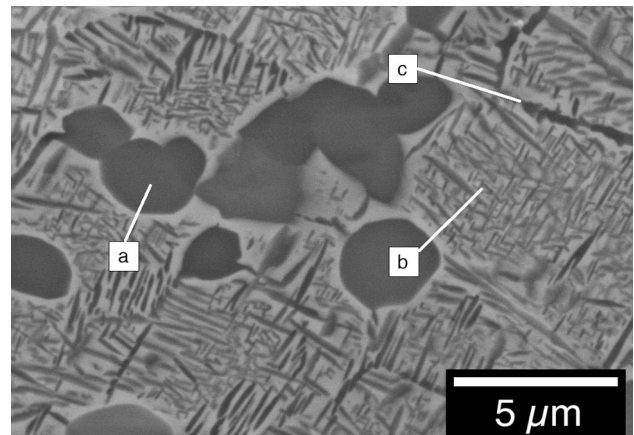


**Figure 2** BSE SEM image showing the typical microstructure of the as-received state of Ti-5553 titanium alloy. (a) nodular  $\alpha$  phase, (b) fine lamellar  $\alpha$  phase, (c) coarse grain boundary  $\alpha$  phase.

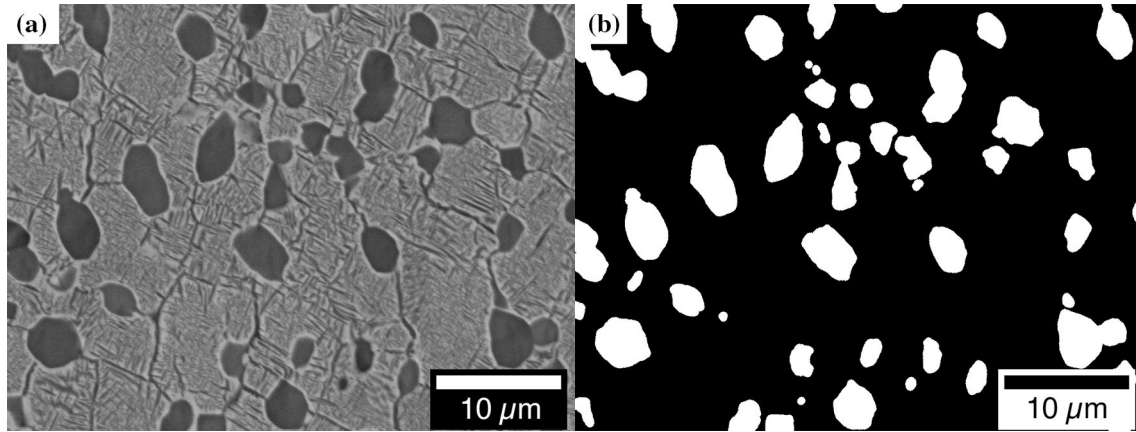


**Figure 3** Gray level image **b** binary image after opening algorithm to determine  $\alpha$  nodules volume fraction in the as-received state of the Ti-5553 alloy.

### Mass fraction of $\alpha$ phase

As an example, Fig. 4 displays the evolution of the experimental diffractograms recorded during heating at a rate of  $10\text{ }^{\circ}\text{C s}^{-1}$ . During heating, only  $\alpha$  and  $\beta$  phases are confirmed (no additional phase was detected whatever the considered heating rate). From room temperature to  $1000\text{ }^{\circ}\text{C}$ , the peak positions of both phases are shifted to lower values of the scattering vector norm, indicating thermal expansion of the phases. Above  $650\text{ }^{\circ}\text{C}$ , an increase in intensity of  $\beta$  peaks is observed while those of  $\alpha$  phase decrease. At the equilibrium  $\beta$  transus temperature, the  $\alpha$  phase dissolution is not complete and only above  $950\text{ }^{\circ}\text{C}$  a complete dissolution of  $\alpha$  phase into  $\beta$  phase happens.

The mass fractions obtained from the Rietveld refinement of the synchrotron diffraction patterns by considering the  $\alpha$  and  $\beta$  phases are provided in Fig. 5 for the three different heating rates (i.e.,  $10\text{ }^{\circ}\text{C s}^{-1}$ ,  $50\text{ }^{\circ}\text{C s}^{-1}$  and  $100\text{ }^{\circ}\text{C s}^{-1}$ ). Only the mass fraction of  $\alpha$  phase is represented and not all data points are shown for readability reasons. The transformations temperature domains are delimited by straight crosses. The mass fraction of  $\alpha$  phase remains relatively constant at low temperature regardless of the considered heating rate. At an intermediate temperature depending on the heating rate, the  $\alpha$  phase dissolution starts. Thus, as the heating rate increases, dissolution starting temperature moved to higher temperatures as well as the dissolution finishing temperature that is higher than  $\beta$  transus temperature ( $861\text{ }^{\circ}\text{C}$ ). In the transformation range, the phase fraction evolutions show two stages in the kinetics of

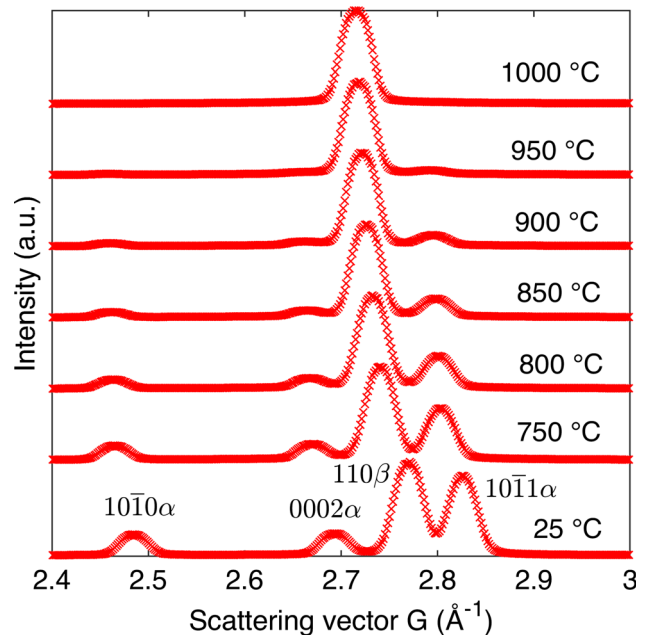


**Figure 4** Synchrotron X-ray experimental diffractograms at various temperatures during heating with a rate of  $10\text{ }^{\circ}\text{C s}^{-1}$  for the first four peaks.

$\alpha$  phase dissolution with faster kinetics in the first stage, at the start of the second stage, with slower kinetics, the remaining  $\alpha$  phase fraction is about 25% for the three heating rates.

Based upon these observations, three different temperatures characterizing the progression of the  $\alpha \rightarrow \beta$  phase transformation have been identified: The dissolution starting temperature  $\tau_s$ , the dissolution finishing temperature  $\tau_f$  and the inflection temperature  $\tau_i$ , which defines the transition between the first and second stages. The starting temperature

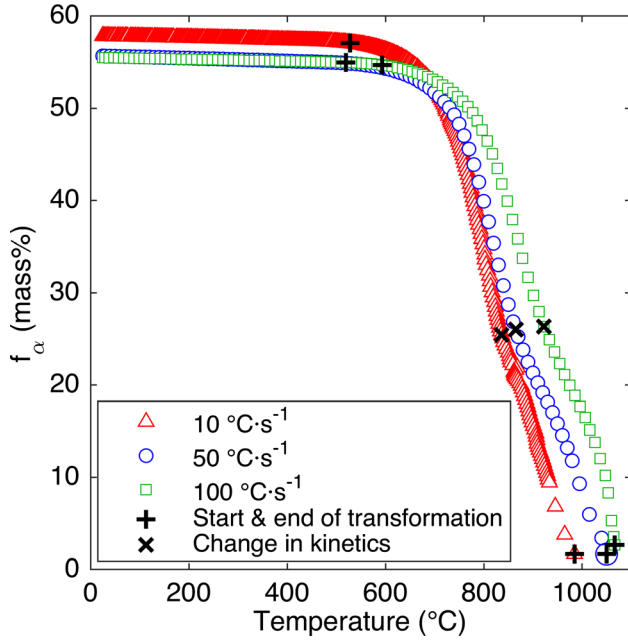


**Figure 5** Mass fraction evolution of  $\alpha$  phase for three heating rates. The beginning and ending of transformation are also reported as well as the inflection temperature marking a slowdown of the transformation kinetics. Not all experimental data points are shown for readability reasons.

corresponds to 1.5% dissolution while the finishing temperature is that at 97% dissolution. The characteristic temperatures are given in Table 1 for each heating rate and reported in Fig. 5.

### Coefficients of total lattice expansion

Figures 6 and 7 show the evolution of the coefficient of total lattice expansion of  $\alpha$  and  $\beta$  phases on heating for the different heating rates, respectively. The values have been derived from the mean lattice parameters evolution with temperature for both phases and the noise has been numerically removed. Lattice parameter variations can be due to different factors such as thermal strain, chemical strain and the extent to which the phase is ordered [37]. In the case of the  $\alpha$

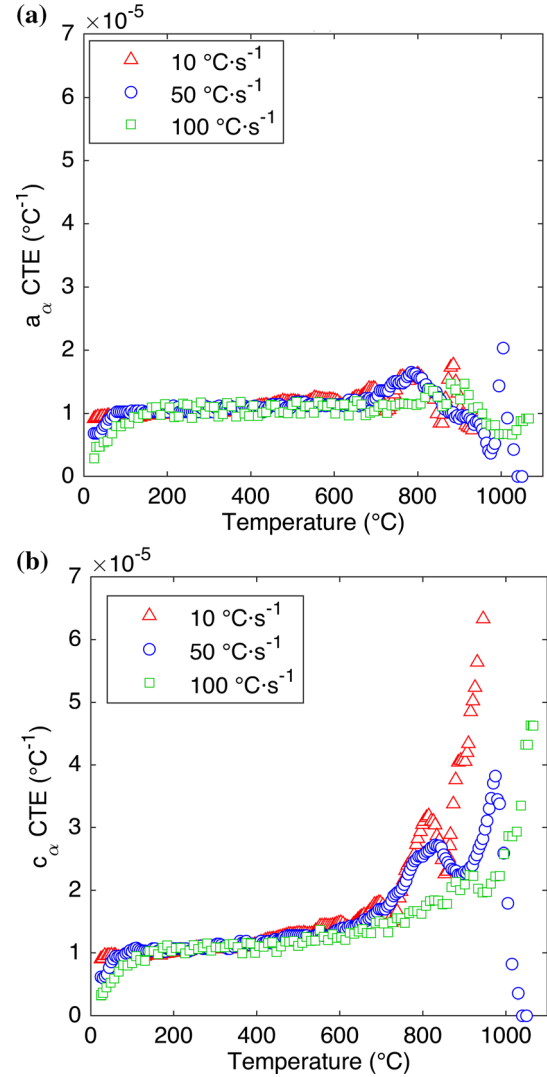


**Figure 6** Evolution of the coefficient of thermal expansion of **a**  $a_\alpha$  and **b**  $c_\alpha$  lattice parameters for the three heating rates.

phase, the coefficient of thermal expansion of both the  $a_\alpha$  and  $c_\alpha$  lattice parameters is nearly constant under 600 °C at a value of  $10 \cdot 10^{-6} \text{ °C}^{-1}$ , which is close to literature data [38]. Above 600 °C, the coefficient of expansion along the  $a_\alpha$  and  $c_\alpha$  directions exhibits a significant increase, followed by a slight decrease and

**Table 1** Dissolution starting temperature ( $\tau_s$ ), finishing temperature ( $\tau_f$ ) and inflection temperature ( $\tau_i$ ) corresponding to change in transformation kinetics for the three heating rates. Two-tangent method was preferred for the determination of the inflection temperatures

	$\tau_s = 1.5\% \text{ (°C)}$	$\tau_f = 97\% \text{ (°C)}$	$\tau_i \text{ (change in kinetics) (°C)}$
$10 \text{ °C s}^{-1}$	527	984	838
$50 \text{ °C s}^{-1}$	520	1050	863
$100 \text{ °C s}^{-1}$	593	1065	920

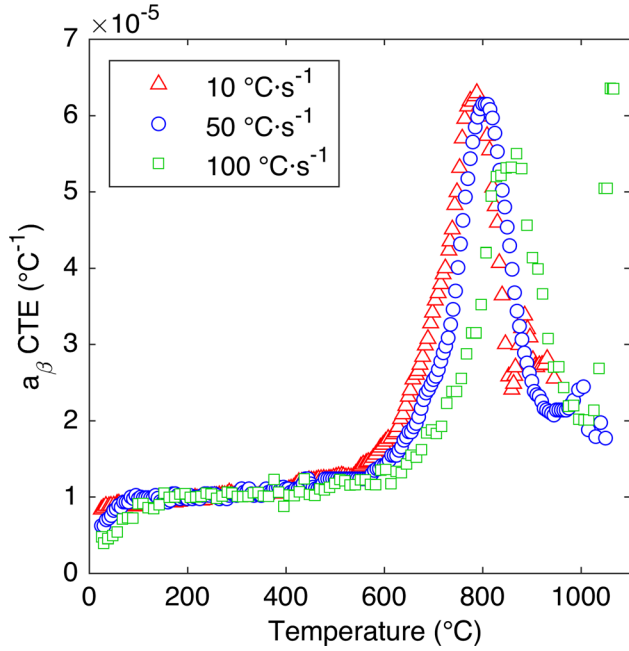


**Figure 7** Evolution of the coefficient of thermal expansion of the  $\beta$  phase lattice parameter for the three heating rates.

finally an increase at high temperatures. Moreover, the coefficient of expansion values reached by the  $c_x$  parameter are much higher than those of the  $a_x$  parameter, indicating an anisotropy between the  $a_x$  and  $c_x$  expansion. It should be noted that the last few data points correspond to a very small remaining  $\alpha$  phase fraction, making the Rietveld refinement difficult for this phase. In the case of the  $\beta$  phase, the coefficient of thermal expansion is also nearly constant up to 600 °C with a value close to  $10 \cdot 10^{-6} \text{ °C}^{-1}$ . Similarly to the  $\alpha$  phase, the  $\beta$  phase coefficient of expansion increases rapidly above 600 °C. It is worth noticing that it is impacted by the dissolution kinetics of the  $\alpha$  phase. In the first stage, where the  $\alpha$  phase dissolution kinetics is faster, the coefficient of expansion of the  $\beta$  phase is higher than  $50 \cdot 10^{-6} \text{ °C}^{-1}$ . In the second stage, where the  $\alpha$  phase dissolution kinetics is slower, it decreases down to a value of around  $20 \cdot 10^{-6} \text{ °C}^{-1}$ .

### Full width at half maximum

The full width at half maximum (FWHM) parameter is an indicator of the phase state (chemical heterogeneity, lattice-distortion and domain size) [39, 40]. To ensure that these variations are related to the phase state, the contribution of non-homogeneous temperature distribution across the sample for the

highest heating rate has been calculated (details are included in Appendix). According to the results, thermal gradients provide a negligible contribution to broadening.

In the present study, the FWHM of  $\{10\bar{1}0\}_\alpha$  and  $\{200\}_\beta$  diffraction peaks have been considered. Figures 8 and 9 display the FWHM changes with temperature for different heating rates and for the  $\{10\bar{1}0\}_\alpha$  and  $\{200\}_\beta$  diffraction peaks, respectively. In the case of the  $\{10\bar{1}0\}_\alpha$  diffraction peaks, the FWHM remains relatively constant with the temperature regardless of the considered heating rate. However, an important increase in FWHM at high temperature should be noted, which can be explained by the decrease of particle size as their dissolution occurs. The offset in the temperature threshold for the lowest heating rate reflects the much lower temperature of complete dissolution (984 °C vs. 1050 and 1065 °C).

Conversely, the FWHM of the  $\beta$  phase exhibits two minima and one maximum. The values of these extrema as well as the corresponding temperatures, depend on the heating rate. Specifically, the amplitudes increase, and the temperatures are shifted toward the high temperatures when the heating rate increases.

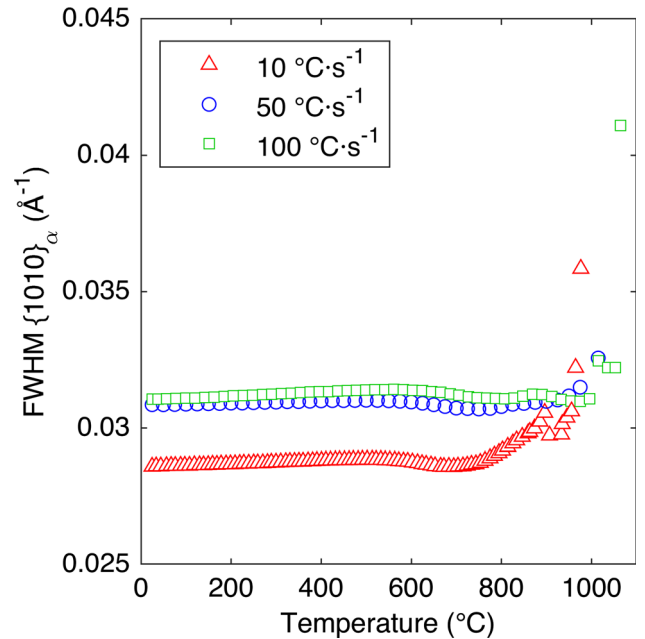


**Figure 8** FWHM evolution of  $\{10\bar{1}0\}_\alpha$  diffraction peaks on heating for different heating rates.

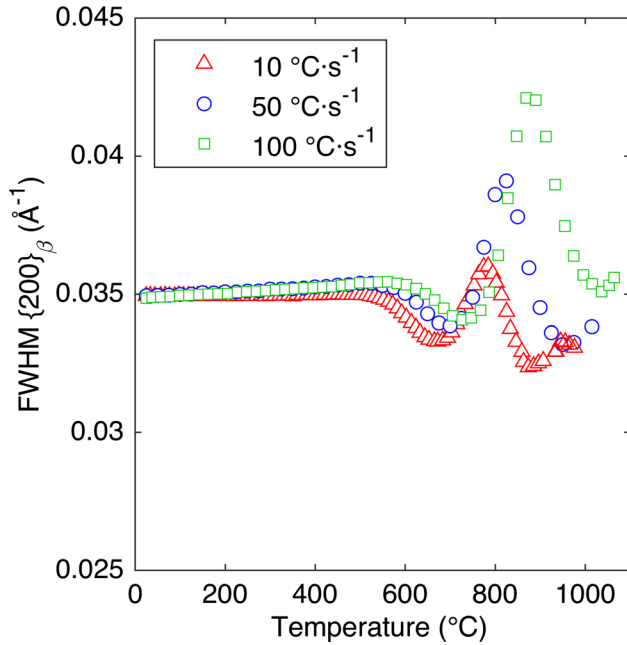


**Figure 9** FWHM evolution of  $\{200\}_{\beta}$  diffraction peak on heating for different heating rates.

## Discussion

In situ high energy X-ray diffraction allows investigating the impact of heating rate on the microstructural changes in the Ti-5553 alloy. Specifically, the experimental setup offers the possibility of monitoring the mass fractions, the mean lattice parameters and the full width at half maximum of the different phases for different heating rates.

For heating rates between 10 and 100  $^{\circ}\text{C s}^{-1}$ , the dissolution of  $\alpha$  phase is divided into two stages that are quite distinct in term of kinetics. This effect can be explained by the presence of nodular and lamellar  $\alpha$  phase morphologies in the initial microstructure. Indeed, the change in dissolution kinetics occurs for a mass fraction of  $\alpha$  phase of about 25%, which is close to the initial  $\alpha$  nodular amount of 21%. As a result, it is expected that, because of the possible differences in chemical composition, strain energy or interfacial energy,  $\alpha$  phase lamellae dissolve faster than  $\alpha$  nodules. To support this hypothesis, a set of samples have been heated at 970  $^{\circ}\text{C}$  (temperature above the inflection temperature and below the dynamic  $\beta$  transus temperature) and then quenched. Figure 10 shows the resulting microstructure, which is composed of  $\alpha$  nodules embedded in the  $\beta$  matrix. Thus, the  $\alpha$  lamellae have been entirely dissolved while a significant amount of  $\alpha$  nodules remains. This finding

is also supported by the work of Barriobero-Vila et al. [11] who found that fine secondary  $\alpha$  lamellae dissolved faster than coarser primary  $\alpha$  precipitates when the Ti-6Al-6V-2Sn alloy is subjected to continuous heating. Dehmas et al. [14] also showed that  $\alpha$  lamellae dissolved faster than  $\alpha$  nodules in a duplex microstructure of the Ti-6Al-4V alloy, further supporting the hypothesis of differentiated transformation kinetics.

The dissolution kinetics of the  $\alpha$  phase has been further investigated by comparing the experimental mass fractions with those predicted at thermodynamic equilibrium. The phase balance in the temperature range of the  $\alpha$  phase dissolution were predicted by using ThermoCalc<sup>®</sup> software [35] and the Saunders database [36]. All solute elements have been included and only the  $\alpha$  and  $\beta$  phases have been considered for the calculation. The comparison with the experimental values for a heating rate of 10  $^{\circ}\text{C s}^{-1}$  is shown in Fig. 11. To confirm the validity of the thermodynamic calculation, a sample has been held at 755  $^{\circ}\text{C}$  during 20 h and then quenched. The  $\alpha$  phase mass fraction for this sample, for which it is assumed that thermodynamic equilibrium was reached after isothermal holding, is also presented in Fig. 11. A good agreement with the thermodynamic calculation is found, suggesting that the Saunders database is suitable for the studied titanium alloy. The experimental values for the heating rate of 10  $^{\circ}\text{C s}^{-1}$  deviate strongly from the thermodynamic calculations. Such results indicate that, unlike the Ti-6Al-4V titanium alloy [10, 14, 15], thermodynamic equilibrium is not reached upon heating even for the lowest heating rate. Ivasishin et al. [41] drew similar

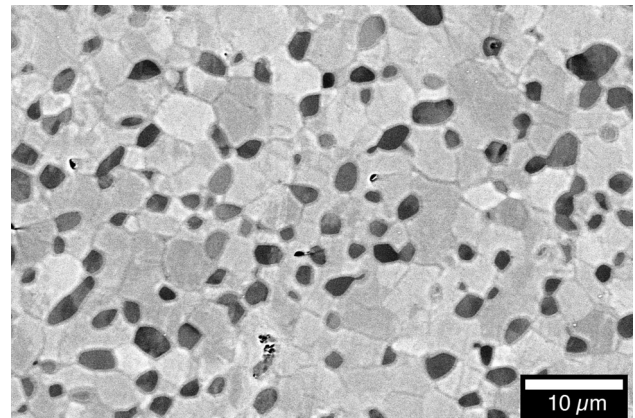


**Figure 10** BSE-SEM image of a Ti-5553 sample heated at 100  $^{\circ}\text{C s}^{-1}$  from room temperature to 970  $^{\circ}\text{C}$  then quenched.



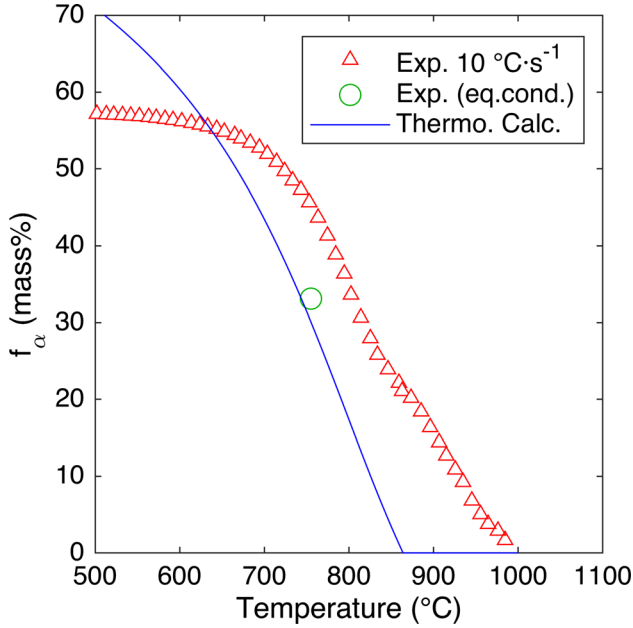


**Figure 11** Comparison of  $\alpha$  phase amount obtained experimentally for heating with a rate of  $10\text{ }^\circ\text{C s}^{-1}$  and numerically at thermodynamic equilibrium (ThermoCalc © with Saunders Database). The green circle gives the mass fraction of  $\alpha$  phase measured after a 20 h holding time at  $755\text{ }^\circ\text{C}$  followed by water quenching.

conclusions on a Russian Ti-5.3Al-2.3Mo-4V-1Fe-1Cr (VT23)  $\alpha + \beta$  alloy. They showed that at high heating rates (near  $100\text{ }^\circ\text{C s}^{-1}$ ), the  $\alpha$  phase can be retained at temperatures above the equilibrium transus temperature. It was determined that the  $\alpha \rightarrow \beta$  transformation is diffusion controlled and dependent on local equilibrium at the  $\alpha/\beta$  interface. In the case of Ti-5553 alloy, most solute elements are present in higher concentrations compared to the VT23 alloy. The data collected by Carman et al. [42] indicate that molybdenum is the solute element with the lowest diffusivity followed by aluminum, vanadium and chromium. Consequently, the slow dissolution kinetics of  $\alpha$  phase compared to the ( $\alpha + \beta$ ) alloys can be interpreted as the result of the presence of molybdenum.

The analysis of the coefficient of thermal expansion provides additional insights for the dissolution mechanism of the  $\alpha$  phase. In the case of the  $\alpha$  phase, the coefficient of thermal expansion in the  $a_x$  and  $c_x$  directions are different in the temperature range when dissolution occurs. According to the literature, this phenomenon is caused by either the anisotropic aspect of thermal expansion in the  $a_x$  and  $c_x$  directions

[43], the increase in the content of interstitial elements (O, N) [44] leading to distortion of the lattice structure. The increase in interstitial content in the  $\alpha$  phase may occur during phase transformation and/or may be due to the initial non-equilibrium contents as shown in ref [45]. The maximum variations of  $\alpha$  phase lattice parameters induced by O and N content variations in the temperature range between  $600\text{ }^\circ\text{C}$  and  $\beta$  transus temperature were calculated considering equilibrium calculation (Thermo-Calc) and Vegard law in ref [46]. The variation amplitudes were found to be  $0.0168\text{ \AA}$  and  $0.1162\text{ \AA}$  for the  $a_x$  and  $c_x$  lattice parameters, respectively. These variation amplitudes are much lower than those observed experimentally. It should be noted that the oxygen and nitrogen contamination is ruled out because the heat treatment has been carried out under secondary vacuum and the probed volume is  $6\text{ mm}^3$ .

In the case of the  $\beta$  phase, a significant change in the coefficient of thermal expansion is observed when  $\alpha$  phase dissolution occurs. According to thermodynamic calculations, the partitioning of  $\beta$ -stabilizers solute elements between  $\alpha$  and  $\beta$  phases is strong. This aspect is illustrated by Fig. 12 which shows the evolution of aluminum  $\alpha$ -stabilizers and molybdenum  $\beta$ -stabilizers solute elements in both phases at thermodynamic equilibrium between  $600\text{ }^\circ\text{C}$  and  $\beta$  transus temperature. Such results indicate that the average content of  $\beta$  stabilizer elements decreases significantly in the  $\beta$  phase. A decrease in the content of  $\beta$ -stabilizing elements in the  $\beta$  phase tends to increase its lattice parameter following Vegard's law [47]. Thus, the variation of the chemical composition of  $\beta$  phase due to the transformation progress can explain the change in coefficient of expansion. This hypothesis is supported by the works of Elmer et al. [10] and Idhil Ismail et al. [15] in the case of the Ti-6Al-4V alloy.

The FWHM analysis of the  $\beta$  phase supports the hypothesis of a diffusional mechanism with a probable non-local equilibrium at the  $\alpha/\beta$  interface. FWHM is sensitive to the average size of the diffraction domains and microstrains. Microstrains can be generated by crystal defects (dislocations) or by local fluctuation in chemical composition (solid solution) [39, 40]. Kabra et al. have also shown that, in the case of neutron diffraction, peaks intensities are related to microstrains induced by dislocations [48]. However, in the present case, because the peak intensities of both  $\alpha$  and  $\beta$  phases change

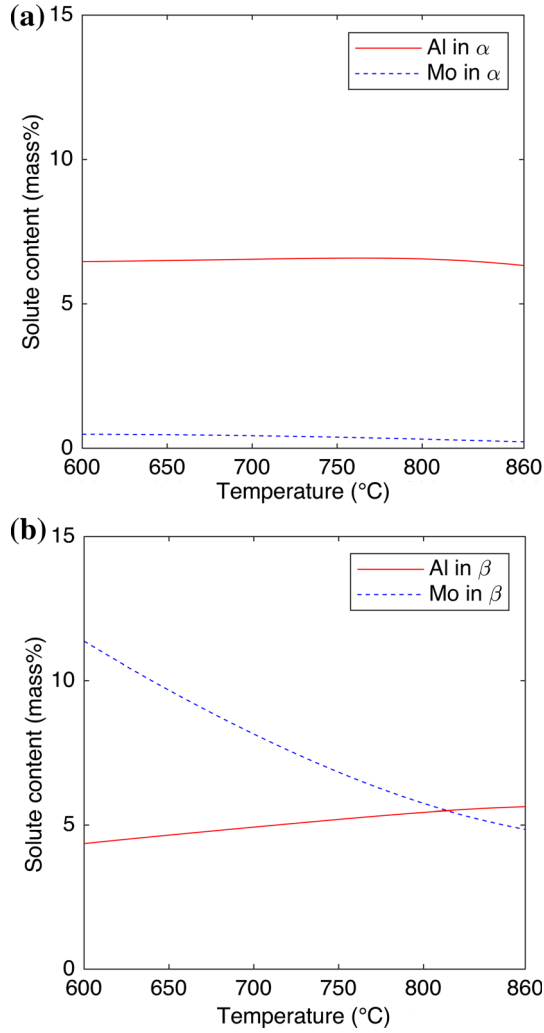


**Figure 12** Evolution of the mass fraction of aluminum  $\alpha$ -stabilizers and molybdenum  $\beta$ -stabilizers solute elements in **(a)**  $\alpha$  phase and **(b)**  $\beta$  phase. The predicted equilibrium values were calculated by using ThermoCalc® software and the Saunders database.

continuously due to the  $\alpha + \beta \rightarrow \beta$  transformation, it is impossible to deconvolute the effect of the phases fractions and the effect of microstrains on peaks intensities. Thus, the Williamson–Hall method [49, 50] has been used to determine the relative impact of each contribution for each heating rate. Figure 13 shows the variations with temperature of the contribution of lattice distortions ( $\varepsilon$ ) and domain size, expressed as  $k\lambda/D$ , where  $k$  is the crystallite shape factor of the Scherrer formula taken at a value of 0.93 [40],  $\lambda$  is the X-ray beam wavelength and  $D$  is the domain size. The results for all heating rates are similar so only the results for a heating rate of  $10\text{ }^\circ\text{C s}^{-1}$  are shown for the purpose of readability.

The Williamson–Hall method shows that the variation of domain size is negligible compared to the variations of microstrains over the whole temperature range of the experiment. To further support this hypothesis the FWHM of the  $\beta$  phase can be plotted as a function of the  $\alpha$  phase mass fraction, as shown in Fig. 14. The FWHM of the  $\beta$  phase starts to decrease when about 1% of the  $\alpha$  phase has dissolved. Consequently, with such quantities of dissolved  $\alpha$  phase, the  $\beta$  domain size increase is very limited and the decrease in FWHM is mostly due to a reduction of  $\beta$  grain stress heterogeneities.

The first increase of FWHM can be explained by the increase in chemical heterogeneity in the  $\beta$  phase when the  $\alpha/\beta$  interface moves. In the temperature range where the FWHM of the  $\beta$  phase increases, the  $\alpha$  phase dissolution mainly involves the fine  $\alpha$ -phase lamellae. As a result, the  $\beta$  phase resulting from the  $\alpha$  phase dissolution first inherits a chemical composition close to that of the  $\alpha$  lamellae, which results in a composition gradient. When the temperature is further increased, the FWHM decreases again. To support this hypothesis the diffusion length ( $L$ ) of molybdenum as a function of temperature has been evaluated. Molybdenum has been chosen because it has the slowest diffusivity of all solute elements, hence it controls the time required to produce a

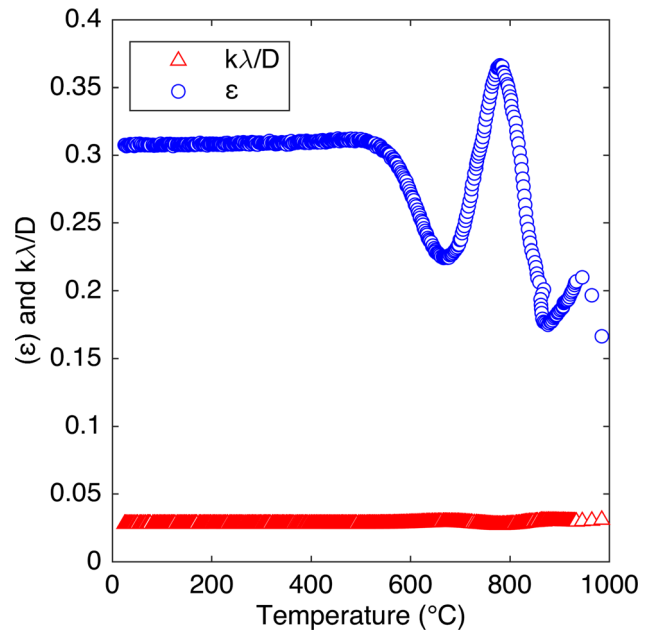


**Figure 13** Variations of the crystal distortions ( $\varepsilon$ ) and domain sizes ( $D$ ) for the  $\beta$  phase upon heating for a heating rate of  $10\text{ }^\circ\text{C s}^{-1}$ .

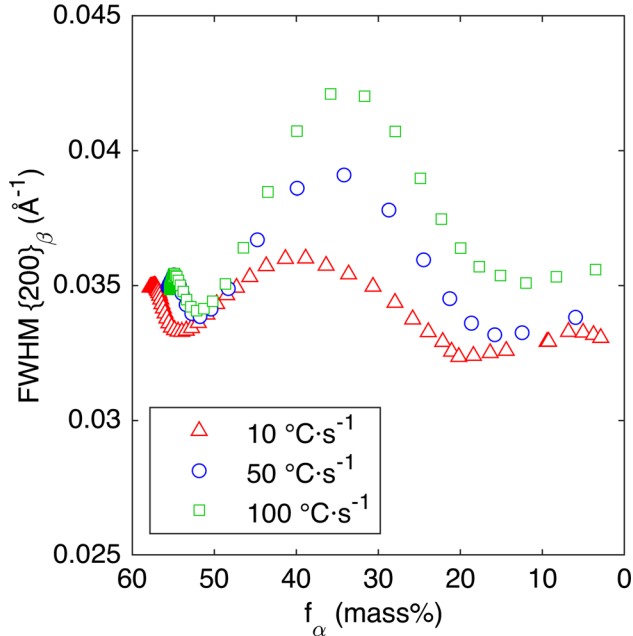


**Figure 14** Evolution of  $\{200\}_\beta$  FWHM versus  $\alpha$  mass fraction on heating for different heating rates.

uniform  $\beta$  composition. For a non-isothermal process, the diffusion length is related to the temperature-dependent diffusivity  $D$  according to:

$$L(t) = \int_{t_0}^t \sqrt{\frac{D(T)}{t}} dt \quad (1)$$

To consider the impact of temperature on diffusivity, the Arrhenius relation is used, that is:

$$D(T) = D_0 e^{-Q/RT} \quad (2)$$

where  $D_0$  is the pre-exponential factor and  $Q$  the activation energy ( $4.87 \cdot 10^{-7} \text{ m}^2 \text{ s}^{-1}$  and  $146.2 \text{ kJ mol}^{-1}$ , respectively, for a Mo content of 5 mass%, according to [51]). In the simulation, the initial value of diffusion length has been fixed to  $0 \mu\text{m}$  at  $500 \text{ }^\circ\text{C}$ , considering that the diffusion is negligible below this temperature. The time step sizes have been set to 0.1 s, 0.02 s and 0.01 s for the 10, 50 and  $100 \text{ }^\circ\text{C s}^{-1}$  heating rates and an explicit Runge-Kutta integration procedure has been used. The molybdenum diffusion length obtained for  $500 \text{ }^\circ\text{C} < T < 1050 \text{ }^\circ\text{C}$  is plotted as a function of temperature in Fig. 15. In the temperature range where the fine  $\alpha$  phase lamellae are dissolved, the diffusion lengths are inferior to 300 nm even for the slowest heating rate. In order to fully homogenize the  $\beta$  phase chemical composition, diffusion length of the

solute elements would need to be at least equal to the half-distance between the center of two  $\alpha$  lamellae, which is about 100 nm for the finest lamellae and up to 400 nm for the coarsest lamellae. Since the diffusion length are short in this temperature range, the mechanism involved in the transformation of  $\alpha$  lamellae would be close to a diffusionless transformation, where the newly formed  $\beta$  phase would inherit a chemical composition close to the parent  $\alpha$  phase, leading to local chemical heterogeneities in the  $\beta$  phase. With an increasing temperature, solute elements are redistributed in the  $\beta$  phase due to longer-range diffusion, resulting in a further decrease of the FWHM. The final increase of the FWHM, which is observed once the  $\alpha$  lamellae dissolution is complete, is related to chemical heterogeneities in the  $\beta$  phase following the dissolution of the nodular  $\alpha$  phase. In that case, the diffusion length required for chemical homogenization of the  $\beta$  phase are higher than that of the  $\alpha$  lamellae with an average distance between nodules of a few micrometers. The amplitude of the last increase in FWHM is lower than the one linked to the dissolution of the  $\alpha$  lamellae. This is expected since the chemical composition gradient in the  $\beta$  phase due to the dissolution of the  $\alpha$  nodules is located near the  $\alpha$  nodule/ $\beta$  matrix interfaces, which

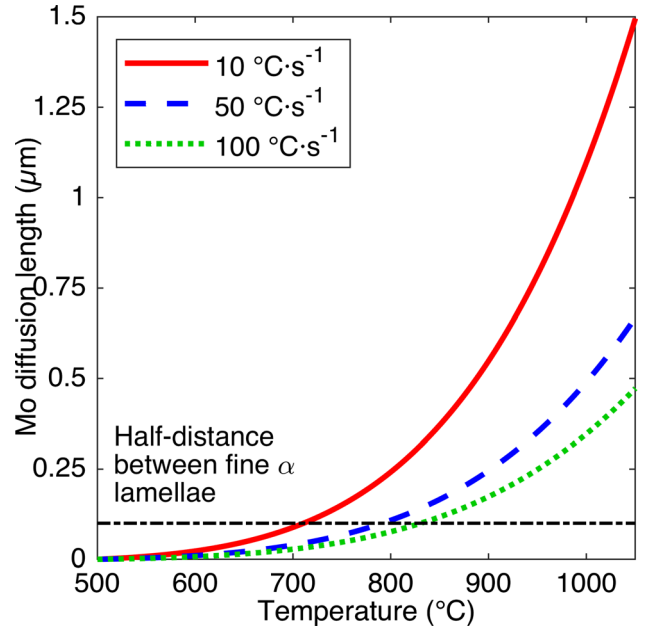


**Figure 15** Mo diffusion length in the  $\beta$  phase versus temperature for three heating rates. Arrhenius law parameters were taken from Kale and Patil. [51]:  $D_0 = 4.87 \cdot 10^{-7} \text{ m}^2 \text{ s}^{-1}$  and  $Q = 146.2 \text{ kJ mol}^{-1}$  for a Mo content of 5 mass%.

represent only a small fraction of the total  $\beta$  phase. The calculated diffusion lengths also show that the diffusion length of molybdenum decreases significantly with an increasing heating rate. This explains why the amplitude of the FWHM variations are higher for the highest heating rate. Indeed, lower diffusion length tend to make the homogenization of the  $\beta$  phase chemical composition slower, and thus, increase the FWHM more.

## Conclusions

The phase transformations of a near  $\beta$  titanium alloy (Ti-5553) with bimodal microstructure subjected to rapid continuous heating from room temperature to 1050 °C have been studied with in situ High Energy X-Ray Diffraction. The following conclusions have been drawn:

- A kinetic effect has been observed with a shift of  $\alpha \rightarrow \beta$  transformation toward high temperatures when the heating rate increases. Thus, for any process involving a heating rate  $\geq 100$  °C s<sup>-1</sup>, no  $\alpha$  phase dissolution takes place until the temperature reaches about 593 °C.
- In the transformation range, two stages in the kinetics of  $\alpha$  phase dissolution, with faster kinetics in the first stage, were highlighted. The first stage is mainly attributed to the dissolution of  $\alpha$  lamellae and the second stage to that of the  $\alpha$  nodules. As discussed, the factors can be numerous, such as the possible difference in chemical composition or in strain energy and  $\alpha/\beta$  interfacial energy between the  $\alpha$  nodules and lamellae.
- The variations of the mean lattice parameters and FWHM during heating suggests that the  $\alpha$  phase dissolution takes place with a diffusional mechanism mainly driven by the  $\alpha/\beta$  interface mobility. The  $\beta$  phase therefore inherits the solute content of the adjacent parent  $\alpha$  phase. This also leads to chemical heterogeneities in the  $\beta$  phase regardless of the considered heating rate.

## Acknowledgements

The authors gratefully acknowledge the French National Research Agency (ANR) under the framework of the DEMUTI project for the financial

support, including all the project partners (TIMET, SECO Tools, LAMPA and LEM3). The authors also acknowledge DESY (Hamburg, Germany), a member of the Helmholtz Association HGF, for the provision of experimental facilities. Parts of this research were carried out at PETRA III and we would like to thank Dr. Norbert Schell for assistance in using the P07 beamline. Beamtime was allocated for proposal I-20190468 EC.

## Author contribution

NC contributed to formal analysis, investigation, writing—original draft and visualization. DP contributed to conceptualization, methodology and writing—original draft. AS contributed to investigation, resources, writing—review and editing. EM contributed to investigation, resources, writing—review and editing. CM contributed to investigation, writing—review and editing. MD contributed to conceptualization, methodology, investigation, writing—original draft, supervision, project administration and funding acquisition.

## Declarations

**Conflict of interest** The authors declare that they have no known competing financial interests or personal relationships that could have appeared to influence the work reported in this paper.

## Appendix

In order to estimate the relative impact of experimental biases related to non-homogenous heating across the sample FWHM, finite element modelling (FEM) were considered with Cast3M [52] software. A two-dimensional axisymmetric finite element model was used to evaluate the thermal gradient through the sample for the three heating rates. Quadratic isoparametric finite elements were used, and an axial symmetry was considered to mesh only half of the 10 mm length of the sample.

A simplified approach in isotropic linear elasticity was chosen and all properties of the material were taken independent of temperature, excepted Young Modulus. But, to overestimate the temperature gradient in the sample, the values have been chosen to minimize thermal conduction and to maximize heat

capacity. The following values were used: thermal conductivity  $5.3 \text{ W m}^{-1} \text{ K}^{-1}$ , heat capacity  $500 \text{ J kg}^{-1} \text{ K}^{-1}$ , volumetric mass density  $4650 \text{ kg m}^{-3}$  [53], coefficient of thermal expansion  $11.10 \cdot 10^{-6} \text{ K}^{-1}$  was taken from this current work, Poisson's ratio of 0.33. Young Modulus was considered to follow the same trend as in J. Baillieux work [54]. Thus, Young Modulus was taken varying linearly from 110 GPa at room temperature [55] down to 60 GPa at 700 °C and 25 GPa at 1200 °C. The heating of the sample is done with an induction coil operating between 80 and 100 kHz. According to Rudnev et al. [56], a penetration depth  $\delta$  can be calculated depending on the inductor frequency, the electrical resistivity  $\rho$  and its relative magnetic permeability  $\mu$ . Values are given in [56] for pure titanium and 70 kHz:  $\delta = 2.25 \text{ mm}$  at 600 °C and 2.55 mm at 1200 °C. As  $\delta$  depends on the inverse of the square root of the frequency, a  $\delta$  value of 1.9 mm would be at least expected for 100 kHz. Furthermore, the electrical resistivity of the Ti-5553 titanium alloy is expected to be higher than the one of pure titanium due to the presence of solute elements increasing  $\delta$  as the square root of electrical resistivity. Consequently, an imposed temperature ramp was applied as thermal loading on the skin of the cylinder on a thickness  $\delta = 1.9 \text{ mm}$  corresponding to the minimal penetration depth.

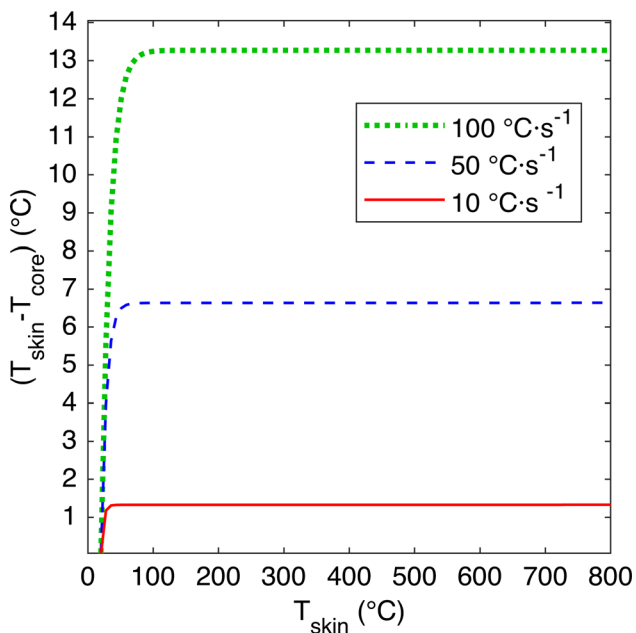


**Figure 16** Evolution of the calculated temperature difference between skin and core of the sample versus imposed skin temperature for each heating rate.

Figure 16 shows calculated temperature difference between the skin and the core of the sample for each heating rate. As expected, the temperature gradient through the thickness was maximal for the fastest heating condition ( $100 \text{ °C s}^{-1}$ ) and reached  $13.3 \text{ °C}$  whereas it was calculated to be below  $1.4 \text{ °C}$  for the slowest heating rate ( $10 \text{ °C s}^{-1}$ ). The temperature gradients increased rapidly up to their respective values before the imposed temperature reached  $150 \text{ °C}$ . Because the temperature differences values are low and constant above  $150 \text{ °C}$ , the experimental setup could not have induced any FWHM variations in the  $\alpha$  dissolution temperature range.

## References

- [1] Lütjering G, Williams JC (2007) Titanium, 2nd edn. Springer, Berlin
- [2] Lütjering G (1998) Influence of processing on microstructure and mechanical properties of ( $\alpha$ + $\beta$ ) titanium alloys. *Mater Sci Eng A* 243:32–45. [https://doi.org/10.1016/S0921-5093\(97\)00778-8](https://doi.org/10.1016/S0921-5093(97)00778-8)
- [3] Banerjee D, Williams JC (2013) Perspectives on titanium science and technology. *Acta Mater* 61:844–879. <https://doi.org/10.1016/j.actamat.2012.10.043>
- [4] Fomin A, Fomina M (2016) FEM modeling and experimental data of induction heating of titanium medical devices. In: 2016 57th international scientific conference on power and electrical engineering of Riga Technical University (RTUCON), pp 1–4
- [5] Markovsky PE, Semiatin SL (2011) Tailoring of microstructure and mechanical properties of Ti–6Al–4V with local rapid (induction) heat treatment. *Mater Sci Eng A* 528:3079–3089. <https://doi.org/10.1016/j.msea.2010.12.002>
- [6] Elmer JW, Palmer TA, Wong J (2003) In situ observations of phase transitions in Ti–6Al–4V alloy welds using spatially resolved X-ray diffraction. *J Appl Phys* 93:1941–1947. <https://doi.org/10.1063/1.1537464>
- [7] Elmer JW, Palmer TA, Babu SS et al (2004) Phase transformation dynamics during welding of Ti–6Al–4V. *J Appl Phys* 95:8327–8339. <https://doi.org/10.1063/1.1737476>
- [8] Rahman Rashid RA, Sun S, Wang G, Dargusch MS (2012) An investigation of cutting forces and cutting temperatures during laser-assisted machining of the Ti–6Cr–5Mo–5V–4Al beta titanium alloy. *Int J Mach Tools Manuf* 63:58–69. <https://doi.org/10.1016/j.ijmactools.2012.06.004>
- [9] Ayed Y, Germain G, Ben Salem W, Hamdi H (2014) Experimental and numerical study of laser-assisted

- machining of Ti6Al4V titanium alloy. *Finite Elem Anal Des* 92:72–79. <https://doi.org/10.1016/j.finel.2014.08.006>
- [10] Elmer JW, Palmer TA, Babu SS, Specht ED (2005) In situ observations of lattice expansion and transformation rates of  $\alpha$  and  $\beta$  phases in Ti–6Al–4V. *Mater Sci Eng A* 391:104–113. <https://doi.org/10.1016/j.msea.2004.08.084>
- [11] Barriobero-Vila P, Requena G, Buslaps T et al (2015) Role of element partitioning on the  $\alpha$ – $\beta$  phase transformation kinetics of a bi-modal Ti–6Al–6V–2Sn alloy during continuous heating. *J Alloys Compd* 626:330–339. <https://doi.org/10.1016/j.jallcom.2014.11.176>
- [12] Malinov S, Sha W, Voon CS (2002) In situ high temperature microscopy study of the surface oxidation and phase transformations in titanium alloys. *J Microsc* 207:163–168. <https://doi.org/10.1046/j.1365-2818.2002.01055.x>
- [13] Semiatin SL, Obstalecki M, Payton EJ et al (2019) Dissolution of the alpha phase in Ti–6Al–4V during isothermal and continuous heat treatment. *Metall Mater Trans A* 50:2356–2370. <https://doi.org/10.1007/s11661-019-05164-6>
- [14] Dehmas M, Katemi R, Appolaire B, et al (2011) Dissolution kinetics of  $\alpha$  phase in TA6V titanium alloy. In: Proceedings of the 12th World conference on titanium, vol 1, pp 719–724
- [15] Ismail AI, Dehmas M, Aeby-Gautier E, Appolaire B (2016) In-situ investigation of phase transformation kinetics in Ti–6Al–4V under rapid heating condition using high-energy synchrotron diffraction. In: Proceedings of the 13th World conference on titanium, pp 591–598
- [16] Callegari B, Aristizabal K, Suarez S et al (2020) In situ evaluation of the low-temperature aging response of Ti–5Al–5Mo–5V–3Cr alloy as influenced by starting microstructure. *J Alloys Compd* 835:155331. <https://doi.org/10.1016/j.jallcom.2020.155331>
- [17] Settefrati A, Aeby-Gautier E, Appolaire B et al (2013) Low temperature transformations in  $\beta$ -metastable Ti 5553 titanium alloy. *Mater Sci Forum* 738–739:97–102
- [18] Aeby-Gautier E, Settefrati A, Bruneseaux F et al (2013) Isothermal  $\alpha''$  formation in  $\beta$  metastable titanium alloys. *J Alloys Compd* 577:S439–S443. <https://doi.org/10.1016/j.jallcom.2012.02.046>
- [19] Barriobero-Vila P, Requena G, Schwarz S et al (2015) Influence of phase transformation kinetics on the formation of  $\alpha$  in a  $\beta$ -quenched Ti–5Al–5Mo–5V–3Cr–1Zr alloy. *Acta Mater* 95:90–101. <https://doi.org/10.1016/j.actamat.2015.05.008>
- [20] Paiotti Marcondes Guimarães R, Callegari B, Warchomicka F et al (2020) In situ analysis of the phase transformation kinetics in the  $\beta$ -water-quenched Ti–5Al–5Mo–5V–3Cr–1Zr alloy during ageing after fast heating. *Quantum Beam Sci* 4:12. <https://doi.org/10.3390/qubs4010012>
- [21] Jones NG, Dashwood RJ, Jackson M, Dye D (2009)  $\beta$  phase decomposition in Ti–5Al–5Mo–5V–3Cr. *Acta Mater* 57:3830–3839. <https://doi.org/10.1016/j.actamat.2009.04.031>
- [22] Thönnessen L (2017) Influence of heat treatment parameters on phase transformations in the near-beta titanium alloy Ti–1Al–8V5Fe. University of Wollongong thesis collection 2017
- [23] Charrier G, Dehmas M, Descoins M, et al (2016) Study of the elemental partitioning for different transformation conditions in the Ti-5553 alloy. In: Proceedings of the 13th World conference on titanium, pp 547–552
- [24] Nag S, Banerjee R, Hwang JY et al (2009) Elemental partitioning between  $\alpha$  and  $\beta$  phases in the Ti–5Al–5Mo–5V–3Cr–0.5Fe (Ti-5553) alloy. *Philos Mag* 89:535–552. <https://doi.org/10.1080/14786430802613158>
- [25] Callegari B, Campo L, Aristizabal K et al (2021) In situ assessment of isochronal phase transformations in a lamellar Ti–5Al–5Mo–5V–3Cr–1Zr alloy using synchrotron X-ray diffraction. *J Alloys Compd* 853:157105. <https://doi.org/10.1016/j.jallcom.2020.157105>
- [26] Gridnev VN, Ivasishin OM, Markovskii PE (1985) Influence of heating rate on the temperature of the ( $\alpha$ + $\beta$ ) $\rightarrow$  $\beta$ -transformation of titanium alloys. *Met Sci Heat Treat* 27:43–48. <https://doi.org/10.1007/BF00741888>
- [27] Schneider CA, Rasband WS, Eliceiri KW (2012) NIH image to ImageJ: 25 years of image analysis. *Nat Methods* 9:671–675. <https://doi.org/10.1038/nmeth.2089>
- [28] Schell N, King A, Beckmann F et al (2014) The high energy materials science beamline (HEMS) at PETRA III. *Mater Sci Forum* 772:57–61
- [29] Liss K-D, Bartels A, Schreyer A, Clemens H (2003) High-energy X-rays: a tool for advanced bulk investigations in materials science and physics. *Textures Microstruct* 35:219–252. <https://doi.org/10.1080/07303300310001634952>
- [30] Rietveld HM (1969) A profile refinement method for nuclear and magnetic structures. *J Appl Crystallogr* 2:65–71. <https://doi.org/10.1107/S0021889869006558>
- [31] Toby BH (2006) R factors in Rietveld analysis: how good is good enough? *Powder Diffr* 21:67–70. <https://doi.org/10.1154/1.2179804>
- [32] Rodriguez-Carjaval J (1990) FullProf: a program for Rietveld refinement and profile matching analysis. Abstracts of the satellite meeting on powder diffraction of the XV congress of the IUCr, Toulouse, France
- [33] Caglioti G, Paoletti A, Ricci FP (1958) Choice of collimators for a crystal spectrometer for neutron diffraction. *Nucl Instrum* 3:223–228. [https://doi.org/10.1016/0369-643X\(58\)90029-X](https://doi.org/10.1016/0369-643X(58)90029-X)

- [34] Stephens PW (1999) Phenomenological model of anisotropic peak broadening in powder diffraction. *J Appl Crystallogr* 32:281–289. <https://doi.org/10.1107/S0021889898006001>
- [35] Andersson J-O, Helander T, Höglund L et al (2002) ThermoCalc & DICTRA, computational tools for materials science. *Calphad* 26:273–312. [https://doi.org/10.1016/S0364-5916\(02\)00037-8](https://doi.org/10.1016/S0364-5916(02)00037-8)
- [36] Saunders N (1998) Titanium database. Thermotech Ltd., Guilford
- [37] Li X, Dippenaar R, Shiro A et al (2018) Lattice parameter evolution during heating of Ti–45Al–7.5Nb–0.25/0.5C alloys under atmospheric and high pressures. *Intermetallics* 102:120–131. <https://doi.org/10.1016/j.intermet.2018.08.011>
- [38] Welsch G, Boyer R, Collings EW (1993) Materials properties handbook: titanium alloys. ASM International, Materials Park
- [39] Scherrer P (1912) Bestimmung der inneren Struktur und der Größe von Kolloidteilchen mittels Röntgenstrahlen. In: Zsigmondy R (ed) *Kolloidchemie Ein Lehrbuch*. Springer, Berlin, pp 387–409
- [40] Patterson AL (1939) The Scherrer formula for X-ray particle size determination. *Phys Rev* 56:978–982. <https://doi.org/10.1103/PhysRev.56.978>
- [41] Ivasishin O, Flower HM (1986) The redistribution of alloying elements by rapid-heating solution treatment of an ( $\alpha + \beta$ ) titanium alloy. *J Mater Sci* 21:2519–2524. <https://doi.org/10.1007/BF01114300>
- [42] Carman A, Zhang LC, Ivasishin OM et al (2011) Role of alloying elements in microstructure evolution and alloying elements behaviour during sintering of a near- $\beta$  titanium alloy. *Mater Sci Eng A* 528:1686–1693. <https://doi.org/10.1016/j.msea.2010.11.004>
- [43] Pawar RR, Deshpande VT (1968) The anisotropy of the thermal expansion of  $\alpha$ -titanium. *Acta Crystallogr A* 24:316–317. <https://doi.org/10.1107/S0567739468000525>
- [44] Jaffee RI (1958) The physical metallurgy of titanium alloys. *Prog Met Phys* 7:65–163. [https://doi.org/10.1016/0502-8205\(58\)90004-2](https://doi.org/10.1016/0502-8205(58)90004-2)
- [45] Yan K, Carr DG, Kabra S et al (2011) In Situ characterization of lattice structure evolution during phase transformation of Zr–2.5Nb. *Adv Eng Mater* 13:882–886. <https://doi.org/10.1002/adem.201000350>
- [46] Wiedemann KE, Shenoy RN, Unnam J (1987) Microhardness and lattice parameter calibrations of the oxygen solid solutions of unalloyed  $\alpha$ -titanium and Ti–6Al–2Sn–4Zr–2Mo. *Metall Trans A* 18:1503–1510. <https://doi.org/10.1007/BF02646662>
- [47] Dobromyslov AV, Elkin VA (2003) Martensitic transformation and metastable  $\beta$ -phase in binary titanium alloys with beta-metals of 4–6 periods. *J Phys IV Proc* 112:723–726. <https://doi.org/10.1051/jp4:2003984>
- [48] Kabra S, Yan K, Carr DG et al (2013) Defect dynamics in polycrystalline zirconium alloy probed in situ by primary extinction of neutron diffraction. *J Appl Phys* 113:063513. <https://doi.org/10.1063/1.4790177>
- [49] Williamson GK, Hall WH (1953) X-ray line broadening from filed aluminium and wolfram. *Acta Metall* 1:22–31. [https://doi.org/10.1016/0001-6160\(53\)90006-6](https://doi.org/10.1016/0001-6160(53)90006-6)
- [50] Nath D, Singh F, Das R (2020) X-ray diffraction analysis by Williamson-Hall, Halder-Wagner and size–strain plot methods of CdSe nanoparticles—a comparative study. *Mater Chem Phys* 239:122021. <https://doi.org/10.1016/j.matchemphys.2019.122021>
- [51] Kale GB, Patil RV (1994) Chemical diffusion in titanium-molybdenum system. *Mater Trans JIM* 35:439–444. <https://doi.org/10.2320/matertrans1989.35.439>
- [52] Hoffmann A, Livolant M, Roche R (1978) CASTEM: a system of finite element computer programs for elastic and inelastic analysis of mechanical structures of reactors. CEA Centre d’Etudes Nucleaires de Saclay
- [53] Wagner V, Baili M, Dessein G, Lallement D (2011) Experimental study of coated carbide tools behaviour: application for Ti-5-5-5-3 turning. *Int J Mach Mach Mater* 9:233. <https://doi.org/10.1504/IJMMM.2011.039649>
- [54] Baillieux J (2015) Effet de l’oxydation sur le comportement mécanique de structures minces en alliages de titane. PhD. thesis, CIRIMAT-ENSIACET
- [55] Bettaieb MB, Hoof TV, Pardoën T et al (2014) On the elastoviscoplastic behavior of the Ti5553 alloy. *Mater Sci Eng A* 617:97–109. <https://doi.org/10.1016/j.msea.2014.08.055>
- [56] Rudnev V, Loveless DL, Cook R (2017) Handbook of induction heating, 2nd edn. CRC Press, New York